FePS₃-MoS₂ *p-n* junctions for broadband optoelectronics

Check for updates

Mei Xian Low[1,2,12], Taimur Ahmed [2,3,12 ✉], Saurabh K. Saini[4,5], Majid Panahandeh-Fard[2,6,7], Joao O. Mendes[8], Anthony S. R. Chesman[8], Chenglong Xu [9], Joel Van Embden[7], Lan Wang[6,7], Mahesh Kumar[2,4], Sharath Sriram[10,11], Madhu Bhaskaran[10,11] & Sumeet Walia [2,3 ✉]

Broadband photodetectors and photovoltaic devices are crucial components in various optoelectronic applications, spanning self-powered photodetectors, solar energy harvesting and optical imaging systems, where optical sensitivity and efficient charge carrier generation are paramount. Two dimensional (2D) materials can be used to form *p-n* junctions for these applications, without crystal lattice or grain boundary constraints, which are common issues in bulk semiconductors. However, a key challenge lies in developing 2D heterojunctions that can efficiently harvest light across a broad spectrum while maintaining high charge separation. Here, we report heterojunctions of iron phosphorus trisulfide (FePS₃) and molybdenum disulphide (MoS₂) as the *p-* and *n*-type materials, respectively, demonstrating broadband photoresponse and photovoltaic behaviour. The results reveal that the FePS₃-MoS₂ heterojunctions form a Type-II band alignment, which not only enhances charge separation at the interface but also leads to faster relaxation times as compared to the individual materials. As such, enabling a robust photovoltaic and photoresponse across the visible spectrum. Notably, the heterojunctions exhibit a short-circuit current density of ~0.29 mA/cm² under visible light and outperform similar two-material heterostructures. These heterojunctions also demonstrate potential for translation onto flexible platforms by maintaining a comparable optoelectronic performance. This opens up opportunities for engineering flexible and self-driven optoelectronic devices, which is beneficial for smart wearable technology.

The *p–n* junction, is well established for its potential applications in photodiodes, photodetectors, photovoltaics, and solar cells based on silicon, germanium, and compound semiconductors[1–7]. Although silicon-based technologies remain the main material for current optoelectronic devices, the miniaturisation of devices with silicon as the active channel material has proven to be complicated by grain boundary constraints[8–10]. To resolve this, two-dimensional (2D) materials have been widely studied in the past two decades as alternatives owing to their superior mechanical and electronic properties at atomic scale thicknesses and lack of grain boundary constraints[11–13].

Recent studies have focused on heterostructuring 2D materials, i.e. combining different 2D materials together to create ultrathin *p–n* junctions[14–16]. This approach is usually difficult to implement with the conventional bulk semiconductors, as the materials structure must be carefully aligned to avoid defects at the interface due to the crystal lattice mismatch[17–19]. Alternatively, heterostructuring 2D materials eliminates this issue, as the 2D materials are typically free from surface dangling bonds and are bound together by weak van der Waals forces, allowing for materials of different compositions, crystal lattices, and intrinsic properties to be heterostructured together[20–22]. The atomically thin nature of these semiconductor 2D materials can further facilitate the transformation from monolithic chips to appropriate flexible substrates, expanding their potential application by reducing their size, weight, and power requirements[23–26].

[1]Integrated Photonics and Applications Centre, School of Engineering, RMIT University, Melbourne, Victoria, Australia. [2]School of Engineering, RMIT University, Melbourne, VIC, Australia. [3]Centre for Opto-electronic Materials and Sensors, RMIT University, Melbourne, VIC, Australia. [4]CSIR-National Physical Laboratory, New Delhi, India. [5]Academy of Scientific and Innovative Research (AcSIR), Ghaziabad, India. [6]ARC Centre of Excellence in Future Low-Energy Electronics Technologies (FLEET), RMIT Node, Melbourne, VIC, Australia. [7]School of Science, RMIT University, Melbourne, VIC, Australia. [8]CSIRO Manufacturing, Clayton, VIC, Australia. [9]MicroNano Research Facility, RMIT University, Melbourne, VIC, Australia. [10]Functional Materials and Microsystems Research Group and the Micro Nano Research Facility, RMIT University, Melbourne, VIC, Australia. [11]ARC Centre of Excellence for Transformative Meta-Optical Systems, RMIT University, Melbourne, VIC, Australia. [12]These authors contributed equally: Mei Xian Low, Taimur Ahmed. ✉e-mail: taimur.ahmed@rmit.edu.au; sumeet.walia@rmit.edu.au

To establish a suitable combination of p- and n-type materials for the desired application, band alignment engineering based on the band energy levels of individual materials are used to ascertain the type of band alignment of the resulting p–n junction[27,28]. Typically, Type-I (straggling) band alignment aids the recombination of charge carriers at the interface for electromagnetic wave emission[29,30]. In contrast, Type-II (staggered) band alignment is advantageous for separating charge carriers, making it suitable for photodetection and photovoltaic applications. Type-II van der Waals heterostructures hold significant promise for self-powered 2D excitonic photodetectors due to their ability to separate electrons and holes between the individual constituent 2D materials, reduced exciton binding energy, and potentially enhanced optical absorbance compared to their standalone components[20,31]. To date, several Type-II heterostructures of 2D materials are reported by carefully forming band alignment engineering and material selection for light-harvesting and self-powered applications[32–36]. However, current self-powered 2D photodetectors face critical challenges, including limited built-in electric fields leading to inefficient charge separation and material constraints due to symmetry[37]. Enhancing photocurrent and excitonic dynamics in heterojunctions remains complex, while ensuring wide-range light detection and stable performance over time. Moreover, integrating these devices onto flexible platforms, are significant barriers to their broader adoption[38,39]. All of this requires investigating different material heterostructures and understanding their interfacial dynamics.

Recent studies have indicated that heterostructuring of iron phosphorus trisulphide ($FePS_3$) and molybdenum disulphide (MoS_2) could provide an avenue to achieve tuneable photoluminescence and photocurrent generation based on the applied voltage[40]. The resulting heterostructure can form either a Type-I or Type-II band alignment based on the thickness-governed band gap of each material, which can be favourable for both enhanced emission or charge separation, respectively. However, due to the lack of consistent band gaps of $FePS_3$ and proximity of band energy levels with MoS_2[41–44], it is challenging to determine which type of band alignment is formed solely based on theoretical estimations alone[45–48].

As multilayer $FePS_3$ and MoS_2 have similar band gaps and broadband optical absorption[42,44], the resulting p-n junction is predicted to possess broadband photovoltaic capabilities in the visible regime of the electromagnetic spectrum. To date, most 2D-material-based p-n junction photovoltaic devices have been explored for single-wavelength photovoltaic applications[49–51]. This can be favourable for applications such as wavelength-selective self-driven photodetectors, however, they are not suitable for broadband photovoltaic detection, which has potential application in optical imaging. One study conducted by Long et al. reported extraordinary photovoltaic performance using MoS_2-graphene-WSe_2 heterostructures[52], which exhibited high broadband current density of ~239 mA/cm² to visible—mid-IR laser irradiation. However, this structure consisted of more than two layers of 2D materials, making the heterostructuring process quite complicated and thus limiting its translation to flexible platforms and scalability.

In this study, we present a simple heterostructure of $FePS_3$ and MoS_2 as the p- and n-type materials, respectively, and investigate its broadband optical response in the visible spectrum[41–44], and demonstrate a broadband photovoltaic device. We have shown that heterostructuring multilayer MoS_2 with $FePS_3$ results in a Type-II band alignment, which improves the charge separation at the junction. The type of band alignment was verified with measurements of the band energy levels of each material, and the enhanced charge separation was also confirmed through excitonic lifetime measurements. These complement the significant reduction in response time of 60 and 99% to illuminations with 565 nm and 660 nm wavelengths observed at the junction, respectively. Furthermore, our heterostructure devices show a broadband photovoltaic response to visible light, where a short-circuit current (I_{SC}) of up to 80 pA (current density of ~0.29 mA/cm²) is exhibited in response to visible wavelength illuminations without any electrical bias, which is comparatively higher than the reported two-materials based photovoltaic heterostructures. Our heterostructure devices can be translated onto flexible platforms as well, opening up opportunities for flexible broadband imaging applications and wearable devices with self-powering capabilities.

Results and discussion
Layout and fabrication of MoS_2/$FePS_3$ p–n heterojunctions

The p–n junction was realised by first heterostructuring mechanically-exfoliated MoS_2 flakes (n-type) on top of $FePS_3$ flakes (p-type) using a wet transfer method on a SiO_2-coated p-doped silicon substrate with polycarbonate as a sacrificial layer, as depicted in Fig. 1a. This was followed by evaporation and patterning of gold (Au) contacts on the heterostructure

Fig. 1 | Structure of heterostructure device. a A schematic illustration of p–n junction device on SiO_2/Si substrate, where MoS_2 was positioned on top of $FePS_3$. **b** Optical micrograph of a representative $FePS_3$-MoS_2 heterostructure device fabricated with electrical contacts. Outline region in white indicates (**c**) the atomic force micrograph region of the heterostructure, where (**d**) the thicknesses of $FePS_3$ and MoS_2 were measured to be 7.2 ± 0.9 nm and 13.4 ± 1.0 nm, respectively.
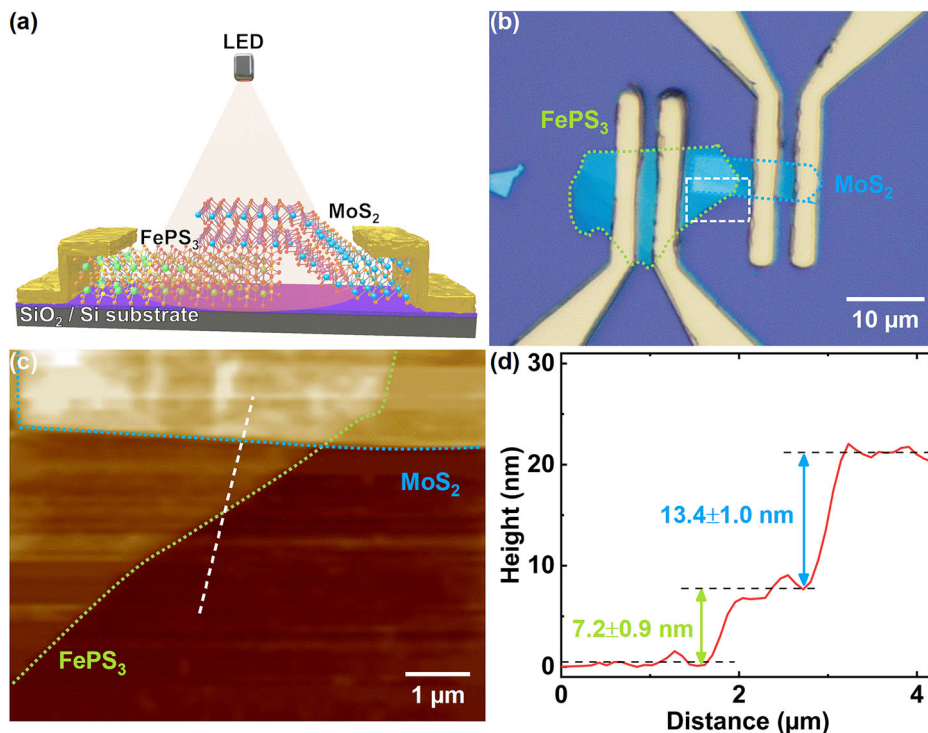
Fig. 2 | Material characterisation of FePS₃-MoS₂ heterostructure. a Raman spectra of FePS$_3$-MoS$_2$ heterojunction (top panel), MoS$_2$ (middle panel) and FePS$_3$ (bottom panel) collected with 532 nm excitation laser and 1800 gr/mm grating. **b** Optical absorbance of FePS$_3$, MoS$_2$, and the heterojunction, where the junction encompasses the absorption range of both FePS$_3$ and MoS$_2$. **c** Photoluminescence (PL) spectra of FePS$_3$ and MoS$_2$ individually (with 405 nm excitation laser), as well as at the heterojunction, which showed quenching of PL.
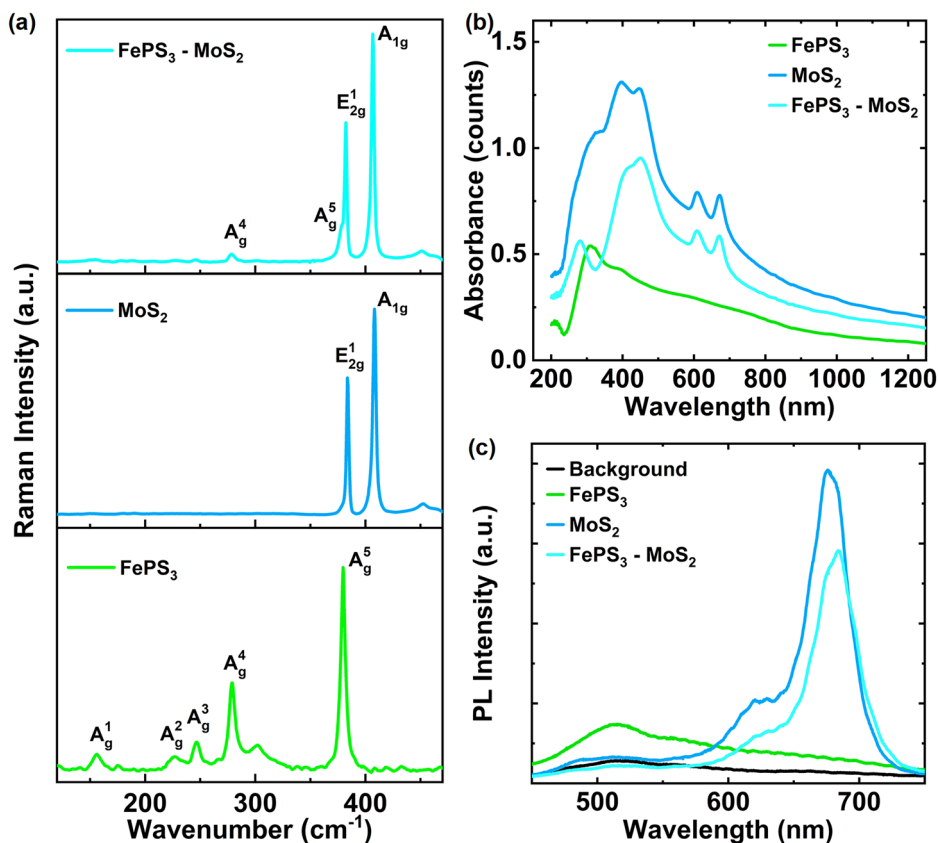
(Fig. 1b), with nickel (Ni) as the adhesion layer (further fabrication details are outlined in the Methods section). Ni was selected as the adhesion layer for the device contacts as its work function is close to the conduction band of MoS$_2$, making it more compatible[53,54]. Prior to studying the electrical properties of the heterojunction, the material properties of the structure were first analysed. Atomic force microscopy (AFM) analysis of the overlapping heterojunction reveals that the FePS$_3$ and MoS$_2$ flakes have thicknesses of 7.2 ± 0.9 nm and 13.4 ± 1.0 nm, respectively (Fig. 1c, d).

Spectroscopic characterisations

Raman spectroscopy was also performed on the individual materials with a 532 nm laser and 1800 g/mm grating (Fig. 2a). FePS$_3$ exhibited multiple phonon modes at 155.9, 226.6, 246.0, 278.6, and 379.6 cm^{-1} (bottom panel, Fig. 2a), which is representative of multilayer monoclinic FePS$_3$[55,56]. MoS$_2$ on the other hand exhibited E$^1_{2g}$ and A$_{1g}$ phonon modes at 380.6 and 405.1 cm^{-1}, respectively, indicating that it is multilayer 2H-MoS$_2$ (middle panel, Fig. 2a)[57,58]. The Raman spectrum of FePS$_3$-MoS$_2$ heterojunction (top panel, Fig. 2a) clearly shows A^4_g and A^5_g modes of FePS$_3$, along with pronounced E$^1_{2g}$ and A$_{1g}$ phonon modes of MoS$_2$. As such, indicating the formation of van der Waals heterojunction. In addition, ultraviolet–visible (UV–Vis) spectroscopy shows both MoS$_2$ and FePS$_3$ to have a broadband optical absorbance from UV to near-infra-red (IR), with peak optical absorbance at ~400 and ~310 nm wavelengths, respectively (Fig. 2b). The heterostructure also demonstrated a broadband optical absorbance of 250–1100 nm with peak absorbances at ~280, 450, 600 and 670 nm owing to a combination of optical absorbances from both individual materials (Fig. 2b). Photoluminescence (PL) characterisation with a 405 nm excitation laser on the individual materials found broad PL peaks centred at 675 and 515 nm, corresponding to MoS$_2$ and FePS$_3$, respectively (Fig. 2c). The observed PL emission from multilayer MoS$_2$ flake may be attributed to the defect-mediated radiative recombination processes, where defect states in the flake act as localised centres for stimulated emission under the illumination of excitation laser[59]. Further, a broad peak around 500 nm present in

all PL spectra, including spectrum from background i.e., SiO$_2$/Si substrate, can be associated with the impurity-related transitions or surface states in SiO$_2$ substrate[60,61]. However, it was observed that the PL intensity of the heterojunction (centred at 680 nm) has been quenched in comparison to the individual materials. The observed PL quenching in the heterojunction provides valuable insights into the band alignment between MoS$_2$ and FePS$_3$. This phenomenon is indicative of a Type-II (staggered) band alignment between the two materials. In a Type-II heterojunction, the conduction band minimum (CBM) and valence band maximum (VBM) of one material are both higher than those of the other material. This configuration promotes the spatial separation of photogenerated electrons and holes, with electrons transferring to the material with the lower CBM and holes to the material with the higher VBM. The resulting charge separation reduces the probability of radiative recombination, leading to the observed PL quenching[62–64].

Broadband optoelectronic characterisations

Optoelectronic characterisations were performed on MoS$_2$ and FePS$_3$ individually, as well as across the heterojunction, where photodetection measurements were performed with a drain-source bias (V_{DS}) of 2 V. The devices were illuminated with monochromatic light sources in visible to near-IR wavelengths (455–1050 nm) and a power intensity (P_{LED}) of 3 m W/cm². When probing the contacts across MoS$_2$ independently, photocurrent generation was observed across a broadband range of light illumination (455–850 nm), with the highest change in photocurrent (i.e. $\Delta I_{DS} = I_{Light} - I_{Dark}$) of ~8.1 μA occurring at 455 nm wavelength (Fig. 3a). However, the photocurrent measured under 850 nm is three orders of magnitude smaller (i.e., on the scale of nano amperes) than visible wavelengths (see Supplementary Fig. 1 in supplementary information). This can be associated with the reduced optical absorbance under the wavelengths higher than 850 nm, as shown by the absorbance profile of MoS$_2$ in Fig. 2b. FePS$_3$ on its own also exhibited broadband photoresponse to light excitation (455–1050 nm), with a relatively comparable photocurrent generation of

Fig. 3 | Photodetection characterisation of FePS₃-MoS₂ heterostructure. Photocurrent generated (ΔI_{DS}) in (**a**) MoS₂ under 455 nm to 850 nm wavelengths, **b** FePS₃ under 455 nm to 1050 nm wavelengths, and **c** the heterojunction when illuminated with wavelengths in 455 nm to 660 nm spectral range. All measurements were performed with a drain-source bias (V_{DS}) of 2 V and LED power intensity of 3 mW/cm². **d** Illumination power-dependent photoresponsivity of FePS₃-MoS₂ heterostructure under 455, 565, and 660 nm wavelengths.
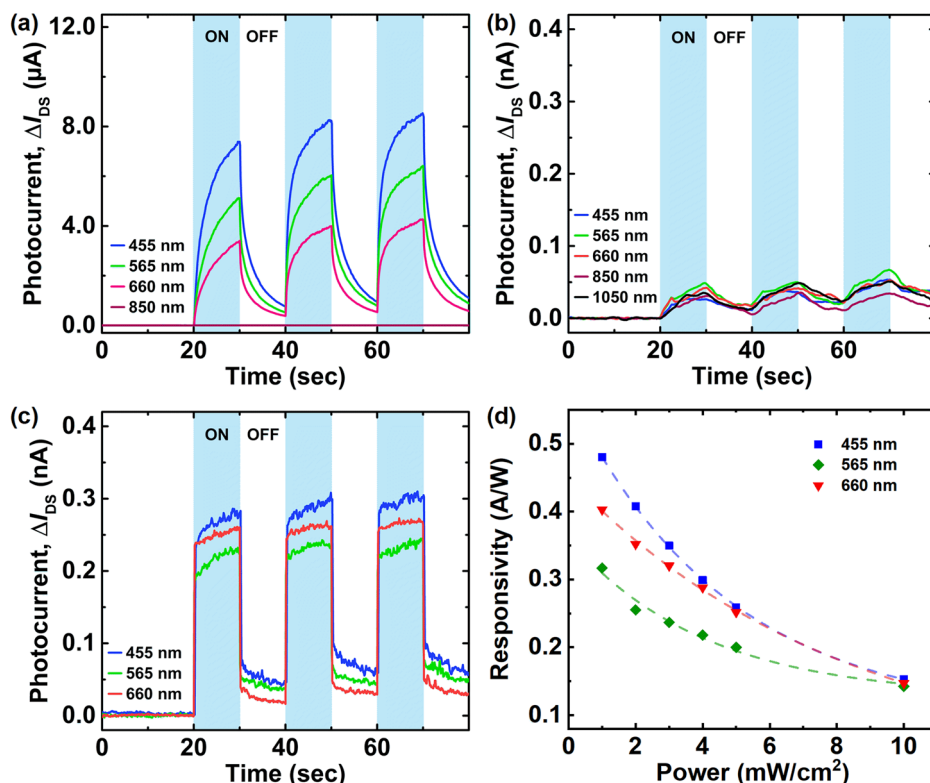
~0.05–0.08 nA across all illumination wavelengths (Fig. 3b). As such, the broadband optoelectronic behaviours and magnitude of photocurrent generated in both MoS₂ and FePS₃ correlate to the optical absorbance range as discussed above in Fig. 2b, where the higher photocurrent observed in MoS₂ compared to FePS₃ is attributed to its higher absorbance in the visible light.

Photoresponse measurements across the heterojunction showed photocurrent generation across a broadband spectral range as well, however, the detection range was narrowed to the visible regime (455–660 nm), with the highest photocurrent of 0.31 nA observed at 455 nm illumination (Fig. 3c). This observation also agrees well with the optical absorbance curve, where the light absorption range of the heterojunction is narrower compared to MoS₂ or FePS₃ individually. Responsivity (R) across different illumination wavelengths is also calculated (using equation $R = \frac{\Delta I_{DS}}{P_{LED} \times A}$)[65–67] to compare the photo-detection properties between MoS₂, FePS₃ and the heterojunction, where ΔI_{DS} is the difference in photocurrent generated ($I_{Light} - I_{Dark}$), P_{LED} is the power density (in W/cm²) of the illumination source, and A is the overlapping heterojunction area[65,68] (calculated to be 27.354 μm² using ImageJ software). Figure 3d shows illumination power-dependent photoresponsivity of FePS₃-MoS₂ heterojunction measured under 455, 565, and 660 nm. The wavelength-dependent responsivity of individual MoS₂ and FePS₃ is plotted in Supplementary information, Supplementary Fig. 2. Comparison of photo-responsivity between the devices shows that although the photoresponsivity across the heterojunction is lower than MoS₂, it is comparable to the photoresponsivity of FePS₃. This could be indicative that the photocurrent generation in the heterostructure was limited by the carrier mobility of FePS₃ (Supplementary information, Supplementary Fig. 3), which inhibits the collection of photogenerated carriers at the electrical contacts[69].

Broadband photovoltaic characterisations
In addition to a broadband photoresponse, the FePS₃-MoS₂ heterojunction also exhibited photovoltaic behaviour, where photocurrent generation was

observed with light excitation without electrical bias ($V_{DS} = 0$ V). ΔI_{DS}–V_{DS} curves across the heterojunction with illumination showed that the photocurrent does not pass through zero at zero bias (Fig. 4a). This observation was further confirmed by transient photocurrent generation observed at the heterojunction with $V_{DS} = 0$ V across a broadband visible spectral range (455 – 660 nm), in which the highest photocurrent of 92 pA was generated at 660 nm (Fig. 4b). To determine the source of the photovoltaic behaviour across the heterojunction, photocurrent mapping was performed on the heterostructure region with a 635 nm laser excitation source. It was revealed that the photocurrent generation seen in the transient response originated from the overlapped heterojunction area (Fig. 4c), indicating that photo-generated carriers were effectively separated without any external bias owing to the presence of the p–n junction. Further confirmation of this phenomenon is shown in Supplementary Fig. 4 (Supplementary information), where photovoltaic behaviour was not observed when only individual materials were probed. Extraction of the short-circuit current (I_{SC}) and open-circuit voltage (V_{OC}) from the ΔI_{DS}–V_{DS} curves is also depicted in Fig. 4d, where V_{OC} is comparable across the different illumination wavelengths, whilst the highest V_{OC} of ~0.28 V and I_{SC} of 80 pA was measured at 660 nm light excitation, which is equivalent to a current density (J_{SC}) of ~0.29 mA/cm². The heterojunction was also subjected to light excitation from a solar simulator (Supplementary Fig. 5), in which a photovoltaic response of ~157 pA (J_{SC} = 1.72 mA/cm²) was observed under the simulated sunlight (1 sun, AM1.5G), indicating potential applicability in solar cell applications.

Charge transport dynamics and type-II band alignment in MoS₂–FePS₃ heterojunctions
To understand the transport behaviour of photogenerated charge carriers across the heterojunction, the rise time (τ_{rise}), i.e. the time required for the generated photocurrent to increase from 10% to 90% in magnitude, between MoS₂, FePS₃, and across the heterojunction of the two materials was measured (see supplementary information, Supplementary Fig. 6). It was observed in Fig. 5a that when comparing the rise times across the different device configurations, the heterojunction had a much lower rise time (>2×) compared to the individual materials. This indicates that the

Fig. 4 | Photovoltaic characterisation of FePS$_3$-MoS$_2$. a ΔI_{DS}–V_{DS} curves of the heterojunction with light excitation ranging from 455 to 660 nm. The inset shows an optical micrograph of the heterojunction area. **b** Photocurrent generated across the FePS$_3$-MoS$_2$ junction when illuminated with illuminations of 455–660 nm and no applied bias (i.e. $V_{DS} = 0$ V). **c** Photocurrent mapping of the heterostructure with 635 nm laser at 0 V bias, indicating the highest photoresponsivity at the overlap region of FePS$_3$ and MoS$_2$. **d** Extracted short-circuit current (I_{SC}) and open-circuit voltage (V_{OC}) of the heterostructure with respect to different illumination wavelengths based on the ΔI_{DS}–V_{DS} curves.
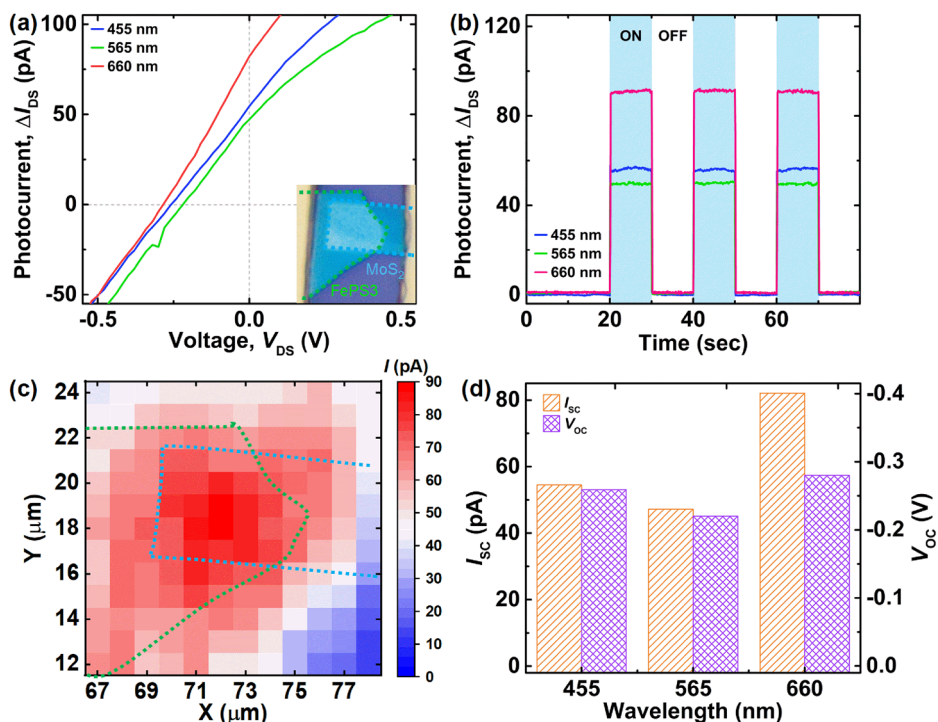

Fig. 5 | Excitonic lifetime measurements of FePS$_3$–MoS$_2$ heterostructure. a Comparison of rise time (τ_{rise}) between MoS$_2$, FePS$_3$, and across the heterojunction. **b** Expected Type-II band alignment of multilayered MoS$_2$ and FePS$_3$ heterostructure, where the valence band maximum (E_{VB}) energy levels were extracted from PESA measurements, whilst the conduction band minimum (E_{CB}) was estimated based on the optical band gaps. Excitonic kinetic comparison of MoS$_2$, FePS$_3$, and across the heterojunction at 545 nm (**c**) without ($V_{DS} = 0$ V) and **d** with electrical bias ($V_{DS} = 2$ V) respectively, where the structure was excited with a 480 nm laser and pump delay of 2.0–2.5 ps.
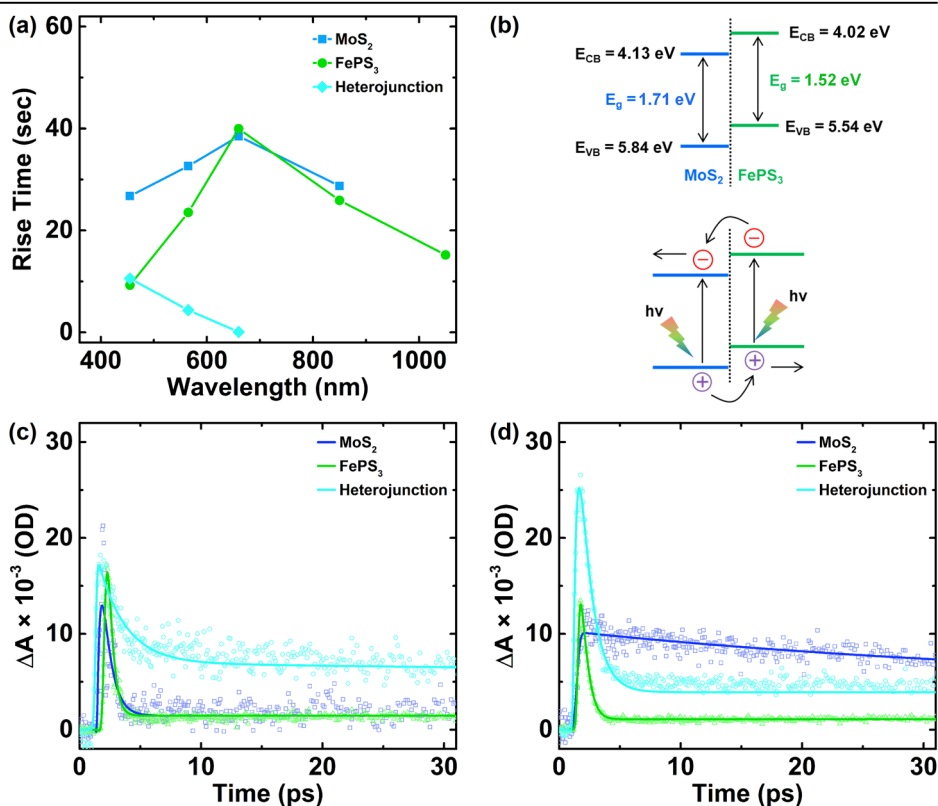
photogenerated charges are being transported more efficiently to the contacts, allowing for steady-state to be achieved rapidly. It is important to mention that the response time of our individual materials might be comparatively slower than the reported literature which could be due to the several parameters such as thickness and quality of materials, excitation wavelength and power *etc*[42,70–72]. However, the primary purpose of comparing the response times of the heterojunction with those of the individual

FePS$_3$ and MoS$_2$ devices (as presented in Fig. 5a) is not to claim superior speed but rather to substantiate the presence of a Type-II band alignment in the FePS$_3$-MoS$_2$ heterojunctions. To validate this observation, the band energy levels of MoS$_2$ and FePS$_3$ were measured using photoelectron spectroscopy in air (PESA) to identify the valence band maximum (E_{VB}), whilst the conduction band minimum (E_{CB}) was estimated based on the optical band gaps (E_{Opt}) of the materials (see supplementary information,

Supplementary Fig. 7). Based on the band energy levels extracted and averaged across multiple measurement values (Supplementary Table 1 in supplementary information), the MoS_2–$FePS_3$ heterojunction was found to form a Type-II band alignment (Fig. 5b). Existing literature has reported that heterostructures with Type-II band alignment show improved charge separation and reduced charge recombination[27,32,73]. Similarly, our heterostructure showed improved charge separation in the form of shorter response times (Fig. 5a), as well as reduced charge recombination based on quenching of PL observed in Fig. 2c. This is indicative that the electrons formed in $FePS_3$ during photonic excitation are able to flow into the conduction band of MoS_2, whilst the holes generated in MoS_2 can transfer into the valence band of $FePS_3$ to be collected at the respective electrical contacts with minimal barriers across the junction. This is further evident from the

illumination power-dependent current–voltage characteristics of heterojunction under 455, 565 and 660 nm wavelengths, as shown in Supplementary Fig. 8. This photoresponse is consistent with the characteristics of photovoltaic effects, where the separation of photoexcited electron–hole pairs are driven by the interfacial built-in electric field at the p–n heterojunction.

In addition to measuring the photoresponse time and defining the band alignment experimentally, excitonic lifetime studies on MoS_2, $FePS_3$, and at heterojunction were performed using femtosecond pump-probe spectroscopy. It was revealed that with a 480 nm excitation laser and no electrical bias applied (Fig. 5c), MoS_2 demonstrated a longer decay time for excited charge carriers to return to the ground state at a 545 nm probe wavelength than either the heterojunction or $FePS_3$ individually (Table 1), with around 7% of the carriers relaxed in 2256 ps. For the heterojunction, 37% of the carriers relaxed in 658 ps, whereas in $FePS_3$, around 29% of carriers relaxed in less than 13 ps. However, after applying a bias to the devices (V_{DS} = 2 V) with the same excitation parameters, the relaxation time for 36% (A3) of the carriers was reduced to 629 ps (Table 2), while the relaxation time for $FePS_3$ was increased to 83 ps for 43% (A2) of the carriers. It is important to note that after applying bias, only 1.3% (A3) of the carriers in the heterojunction have a relaxation time of 1612 ps, but the primary relaxation time (A1 and A2), which comprises the majority of the carriers, was drastically reduced, with 46.5% of the carriers relaxing in 0.36 ps and 52.2% relaxing in 0.78 ps (Fig. 5d). As a result of the perfect coupling between the MoS_2 and $FePS_3$ layers, the majority of carriers relax in a relatively short time frame. The short lifetime suggests a faster recombination rate and consequently a shorter response time, as also seen by the quenching of PL detected at the junction in Figs. 5a and 2d, respectively[30,74,75].

Table 1 | Kinetic lifetimes at 480 nm laser pump and V_{DS} = 0 V.

Device Configuration	Excitonic Carriers [%]		Decay time [ps]		
	A1		A2	t1	t2
MoS_2	92.9		7.1	0.65	2256
$FePS_3$	70.3		29.7	1.23	13.7
Heterojunction	63.0		37.0	2.74	658

Excitonic carrier and decay time comparison between different device configurations.

Table 2 | Kinetic lifetimes at 480 nm laser pump and V_{DS} = 2 V.

Device Configuration	Excitonic Carriers [%]			Decay time [ps]		
	A1	A2	A3	t1	t2	t3
MoS_2	27.7	36.2	36.1	0.83	50.2	629
$FePS_3$	57.2	42.8	-	0.88	83.4	-
Heterojunction	46.5	52.2	1.3	0.36	0.78	1412

Excitonic carrier and decay time comparison between different device configurations.

Flexible platform integration and photovoltaic benchmarking

To investigate the translatability of the heterostructure onto the flexible platforms, $FePS_3$-MoS_2 devices were also fabricated on polyimide (PI) sheets with the same fabrication methods used for the rigid platform (Fig. 6a, b).

Fig. 6 | $FePS_3$-MoS_2 heterostructure on flexible platforms. a Photograph of $FePS_3$-MoS_2 device on a polyimide (PI) sheet, and **b** a zoomed-in optical micrograph of the heterostructure. **c** Photovoltaic behaviour of heterojunction with visible light illumination at 3 mW/cm² power intensity. **d** ΔI_{DS}–V_{DS} curves of the heterojunction on PI, indicating current generation at 0 V bias.
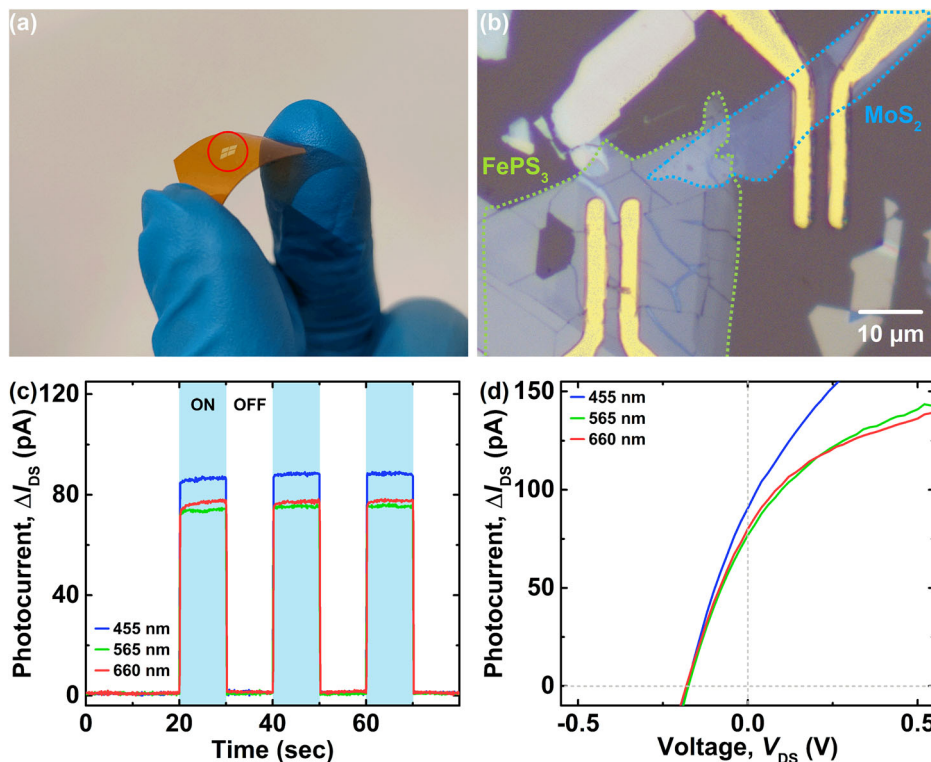
Table 3 | Comparison of broadband photovoltaic performance with existing _p-n_ junction heterostructures utilising 2D FePS$_3$ and/or MoS$_2$.

Device Configuration	Detection Wavelength [nm]	Excitation Power [W]	Responsivity [mA/W]	J_{SC} [mA/cm^2]	V_{OC} [V]	Ref
FePS$_3$-MoS$_2$	455–660	8.3×10^{-10}	480.9	0.29	0.28	This work
FePS$_3$-MoS$_2$	385–850	1.0×10^{-7}	20.0	-	0.25	40
FePS$_3$-MoSe$_2$	400–900	2.5×10^{-7}	52.0	1.21	-	65
FePS$_3$-WS$_2$	405–785	9.4×10^{-5}	32.5	-	0.48	79
MoS$_2$-Ge	360–1000	-	168.5	0.028	0.185	81
MoS$_2$-WS$_2$	532	1.2×10^{-8}	10.4	0.06	0.32	80
MoS$_2$-WSe$_2$	532	7.0×10^{-6}	10	0.85	0.5	82
MoTe$_2$-MoS$_2$	532	7.0×10^{-2}	110.6	-	-	83
MoTe$_2$-MoS$_2$	470–800	3.0×10^{-3}	322.0	0.01	0.11	84
GaSe-MoS$_2$	450–808	1.0×10^{-6}	670.0	95.9	0.62	85
MoS$_2$-Gr-WSe$_2$	400–2400	2.5×10^{-5}	1.0×10^7	~239.0	0.23	52

Similar to the heterostructure on the SiO$_2$/Si substrate, the junction exhibited a photovoltaic response to visible LED illumination at the same power intensity of 3 mW/cm^2. A comparable photocurrent of up to ~87 pA was generated at the heterojunction with zero bias applied (Fig. 6c, d), indicating that the device has a similar photovoltaic performance regardless of whether the junction is on a rigid or flexible platform.

Lastly, to understand the performance of the photovoltaic behaviour exhibited in our FePS$_3$-MoS$_2$ heterojunction, we compared them to existing 2D _p-n_ junction-based heterostructures with broadband photovoltaic properties from the literature (Table 3). It was observed that under a low light intensity of 3 mW/cm^2 (8.3×10^{-10} W) our heterostructure has a slightly lower short circuit current density (J_{SC} of 0.29 mA/cm^2) compared to some of the other _p-n_ junctions. However, when the FePS$_3$-MoS$_2$ heterostructure is exposed to a higher light excitation of 50 mW/cm^2 (1.8×10^{-8} W), it has a slightly higher J_{SC} of 1.72 mA/cm^2 compared to an existing FePS$_3$-MoSe$_2$ heterostructure with similar light excitation power (Supplementary Fig. 9). This is likely attributed to the slightly higher optical absorbance of MoS$_2$ compared to MoSe$_2$ in the visible light regime[76]. The responsivity of our FePS$_3$-MoS$_2$ heterojunction (480.9 mA/W) is comparable to other van der Waals heterostructures, particularly under low excitation power (8.3×10^{-10} W), see Table 3. Although the responsivity of our heterojunctions is lower than recently reported non-photovoltaic heterojunctions involving FePS$_3$ or MoS$_2$, such as β-In$_2$Se$_3$/MoS$_2$ (616.7 A/W)[77], FePS$_3$/ReS$_2$ (41.8 A/W)[33], ReSe$_2$/MoS$_2$ (3.5 A/W)[78], it outperforms systems such as FePS$_3$-MoSe$_2$ (52.0 mA/W)[65], FePS$_3$-WS$_2$ (32.5 mA/W)[79], and MoS$_2$-WS$_2$ (10.4 mA/W)[80] _etc_. It is important to note that the performance of our heterostructure is still much lower than that of a three-layer p-gr-n heterojunction, where the graphene layer facilitates a more efficient charge transfer between the layers. However, this three-layer structure makes it harder for large-area fabrication in the future, and also increases the difficulty in translating the devices onto flexible platforms as well.

In summary, we have successfully fabricated broadband optoelectronic devices based on 2D _p-n_ junctions of FePS$_3$ and MoS$_2$. The fabricated heterojunctions exhibit broadband photoresponse to visible light illuminations of 455 – 660 nm, and also show 60 and 99% faster response under 565 and 660 nm illuminations, respectively, compared to when the individual materials are probed. The faster response time observed at the heterojunction is indicative of enhanced charge transfer, which is facilitated by the experimentally determined Type-II band alignment formed at the junction. In addition, quenching of PL and enhanced carrier relaxation at the junction studied through PL and excitonic lifetime measurements, respectively, also validate the improved charge separation across the heterojunction. The heterostructures can also be translated onto the flexible platforms such as polyimide and retain their broadband optoelectronic performance, demonstrating their potential for application in flexible self-driven optical imaging and smart wearable devices.

Methods
Fabrication of 2D heterostructures
FePS$_3$-MoS$_2$ heterostructure devices were fabricated by first transferring mechanically-exfoliated FePS$_3$ flakes (from commercially purchased bulk crystal, 2D Semiconductors) onto 300 nm thermally oxidised SiO$_2$-coated _p_-doped conductive silicon (Pure Wafer) using a gel film (Gel-Pak). MoS$_2$ flakes (SPI Supplies) were then mechanically exfoliated onto polycarbonate (PC)-coated (HQ Graphene) glass slides, which act as a sacrificial layer in the wet transfer method. This was followed by alignment of the MoS$_2$ flakes onto FePS$_3$ using a transfer stage (HQ Graphene), with the stack then heated to 200 °C for 3 min to melt the PC film. The sacrificial PC layer was then removed by soaking it in chloroform (Sigma-Aldrich) for 2 min. To pattern the electrical contacts on the heterostructures, standard photolithography was performed using a maskless aligner (Heidelberg Instruments MLA150). Electron-beam evaporation (Kurt J. Lesker PVD75) of 10 nm nickel (Ni) and 100 nm gold (Au) was then performed, followed by a lift-off process in an acetone bath to realise electrical contact patterns on the FePS$_3$-MoS$_2$ heterostructures.

Material characterisation
AFM was performed on the heterostructures to identify the thickness of individual flakes using the tapping mode after fabrication of the electrical contacts (Bruker Dimension Icon). Raman and photoluminescence (PL) analysis of the structure was also performed using 532 nm and 405 nm lasers, respectively, at a laser power of 5 mW, 100× objective, and with 1800 gr/mm and 600 gr/mm gratings, respectively (Horiba LabRAM HR Evolution). UV–Vis spectroscopy was also performed on different locations of the heterostructure on a PDMS film with an incident light of 200 nm to 2000 nm and a 5 μm spot size (CRAIC Apollo Microspectrophometer).

Valence/conduction band energy level measurements
The VBM values of MoS$_2$ and FePS$_3$ were obtained via PESA measurements on an AC-2 photoelectron spectrometer (Riken-Keiki Co.). The ionisation energy is determined from the cross point of the photoelectron yield ratio and the UV energy applied (Supplementary Fig. 4). The conduction band minimum (CBM)/work function was measured using a Kelvin probe force microscope (KPFM) in air (Asylum Research Cypher ES). Mechanically exfoliated MoS$_2$ and FePS$_3$ flakes were transferred onto gold-coated silicon substrates, with the CBM values of each material referenced to the underlying gold film (Supplementary Fig. 10 in supplementary information).

Optoelectronic characterisation

Photoresponse characterisations were performed on the heterostructure device using a Keysight 2912B source measurement unit and a vibration-isolated probe station (Everbeing) at ambient conditions (in air at room temperature). All photoresponse characterisations (across MoS_2, $FePS_3$, and heterojunction) were performed with a drain-source bias (V_{DS}) of 2 V. Photovoltaic measurements were performed at a V_{DS} of 0 V. To measure the response of the devices to light, the devices were excited with uncollimated LEDs (Thorlabs Inc.) of various wavelengths (455 nm, 565 nm, 660 nm, 850 nm and 1050 nm) at a power intensity of 3 mW/cm^2 (calibrated with a commercial photodiode, Thorlabs Inc. S120VC). Each cycle of photo-response of the samples was performed with 10 s of illumination, followed by recovery of 10 s.

Excitonic lifetime measurements

Excitonic lifetime measurements were performed on the heterostructures with an ultrafast transient absorption spectroscopy (UFTS) setup, in which the setup comprises a Ti: sapphire-based mode-locked laser oscillator (Coherent Micra) with ~40 fs pulse width, an amplifier (Coherent Legend USP Elite), an optical parametric amplifier (Light Conversion Inc. TOPAS-C), and a spectrometer (Ultrafast Systems Helios). The output laser was passed through a beamsplitter, where the pump beam is pumped through the optical parametric amplifier, whilst the probe beam is passed through an 8 ns long delay stage to provide femtoseconds to nanoseconds temporal delay between the pump and probe.

Data availability

All relevant data are available from the authors upon request.

References

1. Ng, W. L. et al. An efficient room-temperature silicon-based light-emitting diode. *Nature* **410**, 192–194 (2001).
2. Terman, L. M. An investigation of surface states at a silicon/silicon oxide interface employing metal-oxide-silicon diodes. *Solid State Electron.* **5**, 285–299 (1962).
3. Chapin, D. M., Fuller, C. S. & Pearson, G. L. A new silicon p-n junction photocell for converting solar radiation into electrical power. *J. Appl. Phys.* **25**, 676–677 (1954).
4. Aberle, A. G. & Hezel, R. Progress in low-temperature surface passivation of silicon solar cells using remote-plasma silicon nitride. *Prog. Photovoltaics Res. Appl.* **5**, 29–50 (1997).
5. Geisz, J. F. et al. High-efficiency GaInP/GaAs/InGaAs triple-junction solar cells grown inverted with a metamorphic bottom junction. *Appl. Phys Lett.* **91** (2007).
6. Davis, R. F. III-V nitrides for electronic and optoelectronic applications. *Proc. IEEE* **79**, 702–712 (1991).
7. Guo, D. et al. Self-powered ultraviolet photodetector with superhigh photoresponsivity (3.05 A/W) based on the GaN/Sn:Ga_2O_3 pn junction. *ACS Nano* **12**, 12827–12835 (2018).
8. Seto, J. Y. W. The electrical properties of polycrystalline silicon films. *J. Appl. Phys.* **46**, 5247–5254 (1975).
9. Baccarani, G., Riccò, B. & Spadini, G. Transport properties of polycrystalline silicon films. *J. Appl. Phys.* **49**, 5565–5570 (1978).
10. Kurobe, K. I., Ishikawa, Y., Yamamoto, Y., Fuyuki, T. & Matsunami, H. Effects of grain boundaries in polycrystalline silicon thin-film solar cells based on the two-dimensional model. *Sol. Energy Mater. Sol. Cells* **65**, 201–209 (2001).
11. Tan, C. et al. Recent advances in ultrathin two-dimensional nanomaterials. *Chem. Rev.* **117**, 6225–6331 (2017).
12. Akinwande, D., Petrone, N. & Hone, J. Two-dimensional flexible nanoelectronics. *Nat. Commun.* **5**, 5737 (2014).
13. Kang, S. et al. 2D semiconducting materials for electronic and optoelectronic applications: potential and challenge. *2D Materials* **7** (2020).
14. Dutta, T. et al. Electronic properties of 2D materials and their junctions. *Nano Mater. Sci.* **6**, 1–23 (2024).
15. Elahi, E. et al. Contemporary innovations in two-dimensional transition metal dichalcogenide-based P–N junctions for optoelectronics. *Nanoscale* **16**, 14–43 (2024).
16. Mondal, A., Yadav, P. V. K. & Ashok Kumar Reddy, Y. A review on device architecture engineering on various 2D materials toward high-performance photodetectors. *Mater. Today Commun.* **34**, 105094 (2023).
17. Jain, S. C., Harker, A. H. & Cowley, R. A. Misfit strain and misfit dislocations in lattice mismatched epitaxial layers and other systems. *Philos. Mag. A Phys. Condens. Matter, Struct. Defects Mech. Prop.* **75**, 1461–1515 (1997).
18. Jain, S. C., Willander, M. & Maes, H. Stresses and strains in epilayers, stripes and quantum structures of III-V compound semiconductors. *Semiconductor Sci. Technol.* **11**, 641–671 (1996).
19. Koma, A. Van der Waals epitaxy for highly lattice-mismatched systems. *J. Cryst. Growth* **201**, 236–241 (1999).
20. Cao, R. et al. Black phosphorous/indium selenide photoconductive detector for visible and near-infrared light with high sensitivity. *Adv. Optical Mater.* **7** https://doi.org/10.1002/adom.201900020 (2019).
21. Roy, K. et al. Graphene-MoS_2 hybrid structures for multifunctional photoresponsive memory devices. *Nat. Nanotechnol.* **8**, 826–830 (2013).
22. Mudd, G. W. et al. High broad-band photoresponsivity of mechanically formed INSE-graphene van der Waals heterostructures. *Adv. Mater.* **27**, 3760–3766 (2015).
23. Andrzejewski, D. et al. Flexible large-area light-emitting devices based on WS_2 monolayers. *Adv. Optical Mater.* https://doi.org/10.1002/adom.202000694 (2020).
24. Lin, P., Zhu, L., Li, D., Xu, L. & Wang, Z. L. Tunable WSe_2-CdS mixed-dimensional van der Waals heterojunction with a piezo-phototronic effect for an enhanced flexible photodetector. *Nanoscale* **10**, 14472–14479 (2018).
25. Singh, E., Singh, P., Kim, K. S., Yeom, G. Y. & Nalwa, H. S. Flexible molybdenum disulfide (MoS_2) atomic layers for wearable electronics and optoelectronics. *ACS Appl. Mater. Interfaces* **11**, 11061–11105 (2019).
26. Wang, L. & Ang, K. W. *2D Materials for Photonic and Optoelectronic Applications* 117–158 (2019).
27. Franciosi, A. & Van De Walle, C. G. Heterojunction band offset engineering. *Surf. Sci. Rep.* **25**, 1–140 (1996).
28. Özçelik, V. O., Azadani, J. G., Yang, C., Koester, S. J. & Low, T. Band alignment of two-dimensional semiconductors for designing heterostructures with momentum space matching. *Phys. Rev. B* **94**. https://doi.org/10.1103/PhysRevB.94.035125 (2016).
29. Kim, M. S. et al. Enhanced light emission from monolayer semiconductors by forming heterostructures with ZnO thin films. *ACS Appl. Mater. Interfaces* **8**, 28809–28815 (2016).
30. Kuriakose, S. et al. Generating strong room-temperature photoluminescence in black phosphorus using organic molecules. *2D Materials* **6** https://doi.org/10.1088/2053-1583/aae869 (2019).
31. Zhang, K. et al. Interlayer transition and infrared photodetection in atomically thin Type-II $MoTe_2$/MoS_2 van der Waals heterostructures. *ACS Nano* **10**, 3852–3858 (2016).
32. Liu, R. et al. Band alignment engineering in two-dimensional transition metal dichalcogenide-based heterostructures for photodetectors. *Small Struct.* **2**, 2000136 (2021).
33. Gao, H. et al. Enhanced optoelectronic performances of $FePS_3$/ReS_2 Van der Waals heterostructures with type-II band alignment. *Mater. Today Commun.* **35**, 105959 (2023).
34. Zeng, L.-H. et al. Multilayered $PdSe_2$/perovskite schottky junction for fast, self-powered, polarization-sensitive, broadband photodetectors, and image sensor application. *Adv. Sci.* **6**, 1901134 (2019).

35. Huang, L. et al. High-performance self-driven broadband photodetector for polarized imaging based on novel $ZrS_3/ReSe_2$ van der Waals heterojunction. *Mater. Today Nano* **28**, 100527 (2024).

36. Zhu, M. et al. In-situ fabrication of on-chip 1T'-$MoTe_2$/Ge Schottky junction photodetector for self-powered broadband infrared imaging and position sensing. *Nano Res.* **17**, 5587–5594 (2024).

37. Qiao, H. et al. Self-powered photodetectors based on 2D materials. *Adv. Optical Mater.* **8**, 1900765 (2020).

38. Rani, A., Verma, A. & Yadav, B. C. Advancements in transition metal dichalcogenides (TMDCs) for self-powered photodetectors: challenges, properties, and functionalization strategies. *Mater. Adv.* **5**, 3535–3562 (2024).

39. Guan, X. et al. New paradigms of 2D layered material self-driven photodetectors. *Nanoscale* **16**, 20811–20841 (2024).

40. Ramos, M. et al. Tunable, multifunctional opto-electrical response in multilayer $FePS_3$/single-layer MoS_2 van der Waals p-n heterojunctions. *Nanoscale Adv.* **6**, 1909–1916 (2024).

41. Gao, Y. et al. Bias-switchable negative and positive photoconductivity in 2D $FePS_3$ ultraviolet photodetectors. *Nanotechnology* **29**. https://doi.org/10.1088/1361-6528/aab9d2 (2018).

42. Ramos, M. et al. Ultra-broad spectral photo-response in $FePS_3$ air-stable devices. *npj 2D Materials and Applications* **5**. https://doi.org/10.1038/s41699-021-00199-z (2021).

43. Tsai, D. S. et al. Few-layer MoS_2 with high broadband photo again and fast optical switching for use in harsh environments. *ACS Nano* **7**, 3905–3911 (2013).

44. Lopez-Sanchez, O., Lembke, D., Kayci, M., Radenovic, A. & Kis, A. Ultrasensitive photodetectors based on monolayer MoS_2. *Nat. Nanotechnol.* **8**, 497–501 (2013).

45. Ramos, M. et al. Photoluminescence enhancement by band alignment engineering in $MoS_2/FePS_3$ van der Waals heterostructures. *ACS Appl. Mater. Interfaces*. https://doi.org/10.1021/acsami.2c05464 (2022).

46. Hu, C. et al. Work function variation of monolayer MoS_2 by nitrogen-doping. *Appl. Phys. Lett.* **113**. https://doi.org/10.1063/1.5038602 (2018).

47. Zhang, C. et al. Systematic study of electronic structure and band alignment of monolayer transition metal dichalcogenides in Van der Waals heterostructures. *2D Materials* **4** (2017). https://doi.org/10.1088/2053-1583/4/1/015026 (2017).

48. Shlyakhov, I. et al. Energy band alignment of a monolayer MoS_2 with SiO_2 and Al_2O_3 insulators from internal photoemission. *Phys. Status Solidi (A) Appl. Mater. Sci.* **216**. https://doi.org/10.1002/pssa.201800616 (2019).

49. Furchi, M. M., Pospischil, A., Libisch, F., Burgdörfer, J. & Mueller, T. Photovoltaic effect in an electrically tunable Van der Waals heterojunction. *Nano Lett.* **14**, 4785–4791 (2014).

50. Flöry, N. et al. A $WSe_2/MoSe_2$ heterostructure photovoltaic device. *Appl. Phys. Lett.* **107**. https://doi.org/10.1063/1.4931621 (2015).

51. Cho, A. J., Namgung, S. D., Kim, H. & Kwon, J. Y. Electric and photovoltaic characteristics of a multi-layer $ReS_2/ReSe_2$ heterostructure. *APL Mater.* **5**. https://doi.org/10.1063/1.4991028 (2017).

52. Long, M. et al. Broadband photovoltaic detectors based on an atomically thin heterostructure. *Nano Lett.* **16**, 2254–2259 (2016).

53. English, C. D., Shine, G., Dorgan, V. E., Saraswat, K. C. & Pop, E. Improved contacts to MoS_2 transistors by ultra-high vacuum metal deposition. *Nano Lett.* **16**, 3824–3830 (2016).

54. Freedy, K. M. & McDonnell, S. J. Contacts for molybdenum disulfide: Interface chemistry and thermal stability. *Materials* **13**. https://doi.org/10.3390/ma13030693 (2020).

55. Kargar, F. et al. Phonon and thermal properties of quasi-two-dimensional $FePS_3$ and $MnPS_3$ antiferromagnetic semiconductors. *ACS Nano* **14**, 2424–2435 (2020).

56. Wang, X. et al. Raman spectroscopy of atomically thin two-dimensional magnetic iron phosphorus trisulfide ($FePS_3$) crystals. *2D Materials* **3**. https://doi.org/10.1088/2053-1583/3/3/031009 (2016).

57. Chakraborty, B., Matte, H. S. S. R., Sood, A. K. & Rao, C. N. R. Layer-dependent resonant Raman scattering of a few layer MoS_2. *J. Raman Spectrosc.* **44**, 92–96 (2013).

58. Gołasa, K. et al. Resonant Raman scattering in MoS_2—from bulk to monolayer. *Solid State Commun.* **197**, 53–56 (2014).

59. Lin, Y. et al. Enhanced emission from defect levels in multilayer MoS_2. *Adv. Optical Mater.* **10**, 2201059 (2022).

60. Baraban, A. P. et al. Luminescence of SiO_2 layers on silicon at various types of excitation. *J. Lumin.* **205**, 102–108 (2019).

61. Zhao, J. et al. Photoluminescence properties of thermal SiO_2 films implanted by silicon and nitrogen ions. *Nucl. Instrum. Methods Phys. Res. Sect. B: Beam Interact. Mater. At.* **148**, 1002–1006 (1999).

62. Kabongo, G. L. et al. Photoluminescence quenching and enhanced optical conductivity of P_3HT-derived Ho^{3+}-Doped ZnO nanostructures. *Nanoscale Res. Lett.* **11**. https://doi.org/10.1186/s11671-016-1630-3 (2016).

63. Yuan, J. et al. Photoluminescence quenching and charge transfer in artificial heterostacks of monolayer transition metal dichalcogenides and few-layer black phosphorus. *ACS Nano* **9**, 555–563 (2015).

64. Zheng, W. et al. Direct vapor growth of 2D vertical heterostructures with tunable band alignments and interfacial charge transfer behaviors. *Adv. Sci.* **6**. https://doi.org/10.1002/advs.201802204 (2019).

65. Duan, J. et al. Self-driven broadband photodetectors based on $MoSe_2/FePS_3$ van der Waals n-p type-II heterostructures. *ACS Appl. Mater. Interfaces* **14**, 11927–11936 (2022).

66. Ahmed, T. et al. Multifunctional optoelectronics via harnessing defects in layered black phosphorus. *Adv. Funct. Mater.* **29**, 1901991 (2019).

67. Li, Y., Xu, C.-Y., Wang, J.-Y. & Zhen, L. Photodiode-like behavior and excellent photoresponse of vertical Si/monolayer MoS2 heterostructures. *Sci. Rep.* **4**, 7186 (2014).

68. Qi, Z. et al. High-responsivity two-dimensional p-PbI_2/n-WS_2 vertical heterostructure photodetectors enhanced by photogating effect. *Mater. Horiz.* **6**, 1474–1480 (2019).

69. Shoaee, S., Stolterfoht, M. & Neher, D. The role of mobility on charge generation, recombination, and extraction in polymer-based solar cells. *Adv. Energy Mater.* **8**. https://doi.org/10.1002/aenm.201703355 (2018).

70. Jiao, L. et al. Layer-dependent photoresponse of 2D MoS_2 films prepared by pulsed laser deposition. *J. Mater. Chem. C.* **7**, 2522–2529 (2019).

71. Kaushik, V., Varandani, D., Das, P. & Mehta, B. R. Layer dependent photoresponse behavior of chemical vapor deposition synthesized MoS2 films for broadband optical sensing. *J. Phys. D. Appl. Phys.* **52**, 475302 (2019).

72. Wu, J.-Y. et al. Broadband MoS_2 field-effect phototransistors: ultrasensitive visible-light photoresponse and negative infrared photoresponse. *Adv. Mater.* **30**, 1705880 (2018).

73. Jin, C. et al. Ultrafast dynamics in van der Waals heterostructures. *Nat. Nanotechnol.* **13**, 994–1003 (2018).

74. Ahmed, S., Jiang, X., Zhang, F. & Zhang, H. Pump-probe micro-spectroscopy and 2D materials. *Journal of Physics D Applied Physics* **53**. https://doi.org/10.1088/1361-6463/ab77dc (2020).

75. Gabriel, M. M. et al. Direct imaging of free carrier and trap carrier motion in silicon nanowires by spatially-separated femtosecond pump-probe microscopy. *Nano Lett.* **13**, 1336–1340 (2013).

76. Dong, N. et al. Optical limiting and theoretical modelling of layered transition metal dichalcogenide nanosheets. *Scientific Reports* **5**. https://doi.org/10.1038/srep14646 (2015).

77. Li, P. et al. Carrier-recirculating broadband photodetector with high gain based on van der Waals In_2Se_3/MoS_2 heterostructure. *Appl. Surf. Sci.* **649**, 159135 (2024).

78. Li, K. et al. Ultra-fast and linear polarization-sensitive photodetectors based on $ReSe_2/MoS_2$ van der Waals heterostructures. *J. Materiomics* **8**, 1158–1164 (2022).

79. Cao, X. et al. Broadband photodetector based on $FePS_3/WS_2$ van der Waals type II heterostructure. *J. Phys. Chem. Lett.* **14**, 11529–11535 (2023).

80. Wu, W. et al. Self-powered photovoltaic photodetector established on lateral monolayer MoS_2-WS_2 heterostructures. *Nano Energy* **51**, 45–53 (2018).

81. Mahyavanshi, R. D. et al. Photovoltaic action with broadband photoresponsivity in germanium-MoS_2 ultrathin heterojunction. *IEEE Trans. Electron Devices* **65**, 4434–4440 (2018).

82. Lee, C.-H. et al. Atomically thin p–n junctions with van der Waals heterointerfaces. *Nat. Nanotechnol.* **9**, 676–681 (2014).

83. Ji, X. et al. High-performance photodetectors based on $MoTe_2$–MoS_2 van der Waals heterostructures. *ACS Omega* **7**, 10049–10055 (2022).

84. Pezeshki, A., Shokouh, S. H. H., Nazari, T., Oh, K. & Im, S. Electric and photovoltaic behavior of a few-layer $α-MoTe_2/MoS_2$ dichalcogenide heterojunction. *Adv. Mater. ials* **28**, 3216–3222 (2016).

85. He, Z. et al. $GaSe/MoS_2$ heterostructure with ohmic-contact electrodes for fast, broadband photoresponse, and self-driven photodetectors. *Adv. Mater. Interfaces* **7**, 1901848 (2020).

Acknowledgements

Author contributions

M.X.L., T.A. equally contributed to experimental work, data analysis and manuscript preparation. S.K.S. and M.K. carried TRPL experiments and data analysis. M.P.-F. and L.W. collected the photocurrent maps. J.O.M. and A.S.R.C. conducted the optical absorbance experiments. C.X. performed KPFM measurements. J.V.E performed solar simulator photovoltaic measurements. S.S. and M.B. supported with data analysis and contributed to manuscript writing. S.W. conceived the idea and supervised the study. All co-authors commented and provided inputs on the manuscript.

Competing interests

The authors declare no competing interests.

Additional information

Supplementary information The online version contains supplementary material available at https://doi.org/10.1038/s41699-025-00541-9.

Correspondence and requests for materials should be addressed to Taimur Ahmed or Sumeet Walia.

Reprints and permissions information is available at http://www.nature.com/reprints

Publisher's note Springer Nature remains neutral with regard to jurisdictional claims in published maps and institutional affiliations.